Domain pinning near a single-grain boundary in tetragonal and rhombohedral lead zirconate titanate films

D. M. Marincel,[1] H. R. Zhang,[2] J. Britson,[1] A. Belianinov,[3] S. Jesse,[3] S. V. Kalinin,[3] L. Q. Chen,[1] W. M. Rainforth,[2] I. M. Reaney,[2] C. A. Randall,[1] and S. Trolier-McKinstry[1,*]

[1]*Department of Materials Science and Engineering and Materials Research Institute, The Pennsylvania State University, University Park, Pennsylvania 16802, USA*

[2]*Department of Materials Science and Engineering, University of Sheffield, Sheffield S1 3JD, United Kingdom*

[3]*Center for Nanophase Materials Sciences, Oak Ridge National Laboratory, Oak Ridge, Tennessee 37831, USA*

(Received 10 October 2014; revised manuscript received 28 February 2015; published 27 April 2015)

The interaction of grain boundaries with ferroelectric domain walls strongly influences the extrinsic contribution to piezoelectric activity in $PbZr_{1-x},Ti_xO_3$ (PZT), ubiquitous in modern transducers and actuators. However, the fundamental understanding of these phenomena has been limited by complex mechanisms originating from the interplay of atomic-level domain wall pinning, collective domain wall dynamics, and emergent mesoscopic behavior. This contribution utilizes engineered grain boundaries created by depositing epitaxial PZT films with various Zr:Ti ratios onto 24° tilt $SrTiO_3$ bicrystals. The nonlinear piezoelectric response and surface domain structure across the boundary are investigated using piezoresponse force microscopy while the cross-sectional domain structure is studied using transmission electron microscopy. The grain boundary reduces domain wall motion over a width of 800 ± 70 nm for PZT 45:55 and 450±30 nm for PZT 52:48. Phase field modeling provides an understanding of the elastic and electric fields associated with the grain boundary and local domain configurations. This study demonstrates that complex mesoscopic behaviors can be explored to complement atomic-level pictures of the material system.

DOI: 10.1103/PhysRevB.91.134113 PACS number(s): 77.80.Dj, 61.72.Mm, 77.80.bn, 77.55.hj

I. INTRODUCTION

In bulk and thin film ferroelectrics, grain boundaries limit the dielectric and piezoelectric properties, reducing the responses of sensors, actuators, and memory devices [1–4]. Single crystals or epitaxial films cannot always be utilized. Understanding the effect of grain boundaries on domain wall motion is, therefore, essential for controlling device properties. Furthermore, the interaction of domain walls with grain boundaries is vital in describing the fundamental physics of ferroelectric materials.

For over 20 years the interaction between domain walls and grain boundaries has been studied with macroscopic measurements. In 1985 Arlt *et al.* reported decreasing permittivity with grain size below 0.7 μm in $BaTiO_3$ ceramics [5]. Later, measurements of the piezoelectric properties [6,7], Rayleigh response [8]. and field-induced switching indicated decreased extrinsic contribution to the functional properties as grain size decreased [9–11].

Recently, domain wall pinning was studied using phase field models and density functional theory. It was found that stress concentrations and large internal electric fields at grain boundaries and triple points influence both domain nucleation and domain wall pinning [12–15]. Additionally, a preference for specific polarization directions on either side of high-angle grain boundaries may produce pinning [16]. Significant charge concentrations can exist at 90° domain walls, which then exert a local pressure on 180° domain walls even at subswitching electric fields due to variations in the local electric field [17,18].

Experimentally, PFM measurements demonstrated that one- and two-dimensional defects produce significant pinning of 180° domain walls in ferroelectric films [19–24]. The local electric field created by defects and domain wall–domain wall pinning are the major contributions to domain wall pinning [17,25]. It is widely reported that in tetragonal ferroelectrics the domain structures of adjacent grains are correlated due to local strain and electric fields [2,26]. Ivry *et al.* indicate that the local fields influence the domain structure up to 300–400 nm from the grain boundary [26], a result matching the distance observed for the influence of a grain boundary on domain wall motion [27].

The contribution of domain wall motion to the dielectric and piezoelectric properties is dependent on composition and crystallographic structure [4,28–31]. The highest irreversible domain wall motion is observed at the morphotropic phase boundary and decreases as internal stress increases with increasing ferroelastic strain [28,29,32]. However, the role of ferroelectric distortion (e.g., rhombohedral, tetragonal, etc.) on domain wall interaction with planar defects is unknown. Recently, 24° tilt grain boundaries were shown to pin domain walls in tetragonal $PbZr_{0.45}Ti_{0.55}O_3$ (PZT 45/55) films and reduce domain wall motion ∼350 nm to either side of the grain boundary, with strong dependence on the local domain structure [27]. It is anticipated that the relative pinning strength of any particular grain boundary will depend on the accommodation of the local strain by the ferroelectric domain structure.

This work explores the effect of ferroelastic strain on the domain structure and local piezoelectric nonlinearity at and near the grain boundary. Comparisons are made between tetragonal and rhombohedral epitaxial PZT thin films with 24° tilt grain boundaries. Particular emphasis is placed on the spatial width of reduced or enhanced nonlinear response resulting from the grain boundary.

*Corresponding author: N-227 Millennium Science Complex, University Park, Pennsylvania 16802, USA; stmckinstry@psu.edu

II. MATERIALS AND METHODS

A. Material synthesis

Bicrystal (100) $SrTiO_3$ substrates with a 24° tilt angle (MTI Corp.) were used to engineer a well-defined grain boundary. A $SrRuO_3$ buffer layer was deposited as a bottom electrode followed by deposition of the $PbZr_{1-x}Ti_xO_3$ films, with compositions $x = 0.80$, 0.55, and 0.48. All samples were prepared as described previously [27].

Electrical measurements of capacitance and dielectric loss (HP 4284A Precision LCR Meter) were made as a function of ac voltage to 50% of the coercive voltage to determine the dielectric nonlinearity $\alpha_\varepsilon/\varepsilon_{\text{init}}$. The Rayleigh law describes the contribution of domain wall motion across pinning sites [33]. Further information on the Rayleigh law is provided in Appendix A. Concisely, the initial response ($\varepsilon_{\text{init}}$, $d_{33,\text{init}}$) relates to the intrinsic response and reversible domain wall motion, while the irreversible response (α_ε, α_d) relates to irreversible domain wall motion.

B. Band excitation piezoresponse force microscopy (BEPFM)

BEPFM characterization of the *local* piezoelectric nonlinear response (Cypher, Asylum Research, Inc.) was made on a $5\mu m \times 5\,\mu m$ region with a 100×100 pixel grid in a 100 kHz band across the resonant frequency of the cantilever (PPP-EFM-50, NanoSensors). Samples were poled at 230 kV/cm for 40 min for PZT 20/80, 310 kV/cm for 15 min for PZT 45/55, and 98 kV/cm for 35 min for PZT 52/48 and aged for 30 min prior to measurement. Poling parameters were determined using the global piezoelectric response (aixDBLI, aixACCT Systems). The capacitors were driven from the bottom, with tip and top electrode grounded. The drive voltage extended beyond the dielectric Rayleigh regime, as this was necessary in order to minimize noise. Thus, the reported values for nonlinear response are the ratio of the quadratic to linear response normalized to the film thickness [27]. Methods for analyzing the clusters of nonlinear response are described in Appendix B.

C. Transmission electron microscopy (TEM)

TEM provided information on the domain structure at and away from the grain boundary. Specimens were prepared with a dual beam focused ion beam scanning electron microscope (SEM) (Quanta 3D 200, FEI). SEM was used to locate the grain boundary, then cross-section and plan-view TEM specimens containing the grain boundary were prepared. Micrographs were collected with a field emission JEOL 2010F JEOL 2010 scanning transmission electron microscope operated at 200 kV. The specimens were rotated (925 double tilt rotation analytical holder, Gatan) to orient the grain boundary vertical in the CCD camera image. The 24° bicrystal specimens were tilted to the symmetric condition with each grain 12° off the [100] zone axis for comparing the domain structures across the grain boundary.

D. Phase field modeling

Phase field modeling [13,34–36] was used to investigate the structure and relative stability of the domain configurations around the 24° tilt grain boundaries. The models provided additional insight into the electrostatic and mechanical state of the thin film as well as the domain width around the grain boundary. Details for the numeric modeling approach are presented in Appendix C. Two domain structures near the grain boundaries were used as inputs for the model to determine similar equilibrium structures: the a/c structure with the in-plane polarization nearly parallel to the grain boundary and the b/c structure with the in-plane polarization nearly perpendicular to the grain boundary. Films with the a/c domain structure were simulated on a discrete grid of $256\Delta x \times 128\Delta x \times 54\Delta x$ while the film with the b/c domain structure was simulated on a grid of $120\Delta x \times 320\Delta x \times 54\Delta x$ with a resolution of $\Delta x = 0.5$ nm. Periodic boundary conditions in the first two dimensions and appropriate boundary conditions to simulate the thin films in the third dimension were used in the model, as described in Appendix C. Different film dimensions were used to accommodate the periodicities of the two domain structures. The thin film for both models was 15 nm thick with a nonpolarizable 7-nm-thick layer of deformable substrate allowed to relax beneath the film [35]. To model the bicrystal system, the anisotropic system properties were rotated in each grain to accommodate the 24° rotation between the crystals. Between grains the properties were assumed to vary smoothly across the boundary and, since the width of the boundary has not been exactly established, we assumed the transition occurred over a distance of 2 nm.

Electrostatic interactions between domains arising from the electric field were included through explicit consideration of the electrostatic energy in the model. Electric fields in the system arising from bound charges caused by changes in the polarization at the domain walls were found by solving the Poisson equation assuming electrodes on the film to be ideally compensating and electrically grounded [37]. When considering thin films with only b/c type domain structures and consequently highly charged grain boundaries in PZT 20/80 films, however, we also considered the additional case of free charge carriers in the film fully compensating the bound charges around the domain walls due to the lower band gap of PZT 20/80. This allows the effects of two extremes in the electric behavior of the thin films on the domain structures around the grain boundary to be considered. Mechanical stresses in the thin films due to the spontaneous deformation of the crystal during the ferroelectric transition were similarly determined by solving the mechanical equilibrium equations in the film as discussed in Refs. [35,38] and in Appendix C.

III. RESULTS

Films were grown to a thickness of 481 nm for PZT 20/80, 425 nm for PZT 45/55, and 791 nm for PZT 52/48. X-ray diffraction showed phase pure tetragonal (PZT 20/80 and PZT 45/55) and rhombohedral (PZT 52/48; see Appendix D) films with $\langle 001\rangle/\langle 100\rangle$ out of plane. Phi scans of the PZT 101 peak proved epitaxy on both sides of the grain boundary. The full width at half maximum for the PZT 002 peak rocking curve, along with the permittivity, loss tangent, and remanent polarization for all compositions are provided in Table I. The measurements indicate high film quality.

Global dielectric Rayleigh measurements and averaged local piezoelectric nonlinearities are presented in Table II.

TABLE I. Structural and electrical data for PZT films of different composition.

Composition	PZT 002 FWHM (deg ω)	ε_r (10 kHz, 30 mV)	$\tan\delta$ (%)	P_r (μC/cm^2)
PZT 20/80	1.19	224	0.8	44.5
PZT 45/55 [22]	0.60	456	1.0	41.0
PZT 52/48	0.11	413	1.0	37.1

As expected, the highest initial permittivity was observed for the composition near the morphotropic phase boundary (PZT 52/48). However, the highest $\alpha_\varepsilon/\varepsilon_{\text{init}}$ was observed for PZT 45/55, followed by PZT 20/80 and PZT 52/48, similar to the trend observed in the averaged local nonlinear piezoelectric response. These results suggest that a larger percentage of the domain walls in PZT 52/48 are reversibly excited, resulting in a higher reversible component and a lower irreversible component than PZT 45/55.

Band excitation piezoresponse force microscopy (BEPFM), Figs. 1(a)–1(c), was used to collect maps of nonlinear response across the grain boundaries. For all three compositions there is a *local* minimum in the average nonlinear response at the grain boundary [Figs. 1(d)–1(f)], indicating that a 24° grain boundary reduces the nonlinear response for all compositions. The average width of the reduced nonlinear response for PZT 45/55 is 800 ± 70 nm and for PZT 52/48 is 450 ± 30 nm, $\sim$2–3$\times$ larger than the observed cluster size far from the grain boundary (240 ± 30 nm for PZT 45/55 [27] and 200 ± 90 nm for PZT 52/48). The decreased width of reduced response for PZT 52/48 relative to PZT 45/55 is attributed to improved relaxation of the strain and electric field associated with the grain boundary, possibly because of the higher domain wall density. Previous measurements on 24° tilt grain boundaries in PZT 45/55 films of various thicknesses showed no significant variation in the width of reduced response [27], indicating that the different width of reduced nonlinear response for PZT 52/48 relative to PZT 45/55 is unlikely to be an artifact of the different thicknesses.

For PZT 20/80, the nonlinear response at the grain boundary varies spatially. Although no *global* minimum in response is observed at the grain boundary for PZT 20/80, on average there is reduced coupling of high nonlinear response from one side of the grain boundary to the other. As seen in Fig. 1(a), $\sim$28% of the grain boundary has nonlinear response more than half a standard deviation above the mean, indicating some coupling of domain wall motion across the boundary. However, the remainder of the grain boundary shows a significantly lower nonlinear response than that observed immediately adjacent to the grain boundary, indicating that the grain boundary primarily acts to reduce concerted domain wall motion.

To probe the underlying reasons behind the local nonlinear response, transmission electron microscopy (TEM) was used to determine the domain structure as a function of distance from the grain boundary. For the analysis of tetragonal films, *a* domains are those with polarization in the plane of the film and nearly parallel to the grain boundary, *b* domains have polarization nearly perpendicular to the grain boundary, and *c* domains have polarization perpendicular to the film surface. Cross-sectional TEM provides information on how domain patterns extend through the film thickness. Figures 2(a)–2(f) provide micrographs of all films (a–c) before and (d–f) after poling. For both tetragonal compositions, all domain variants are observed $>$500 nm from the grain boundary. Near the grain boundary, PZT 20/80 had a combination of *b* and *c* domains, while PZT 45/55 exhibited primarily *a* and *c* domains. PZT 52/48 showed a fine domain tweed structure attributed to reduced domain wall energy near the morphotropic phase boundary [39].

Vertical PFM amplitude measurements of the domain structure off the capacitor and prior to poling are shown in Figs. 2(g)–2(i) with *c* domains evident as bright (high-response) regions while *a* and *b* domains are both evident as dark (low-response) regions. Figures 2(g) and 5(a) show that the domain variants observed by PFM are similar to those in plan-view TEM. The PFM images show that the surface domain structures change along the grain boundary. A combination of all three ferroelastic domain variants for PZT 20/80 and 45/55 are evident. Note that for PZT 52/48 the out-of-plane response amplitude should be uniform in an ideally poled sample. The dark regions represent domain boundaries between regions with opposite out-of-plane phase response.

Phase field modeling was employed to understand the forces controlling domain structure development at the grain boundary. To model the case where *a* and *c* domains cross the grain boundary, the system was initialized with four 90° domain walls oriented perpendicular to two grain boundaries. When allowed to relax, the domain walls rotated 12°, producing a stable configuration along the $\langle 101 \rangle$ plane in each grain as shown in Fig. 3(a), similar to the PZT 45/55 domain structure described previously [27]. In addition, the domain walls also bend towards the grain boundary, with most bending near the

TABLE II. Composition dependence of dielectric and piezoelectric nonlinear response measured at 300 kHz.

	Dielectric Rayleigh parameters			BE-PFM quadraticlinear	
Composition	$\varepsilon_{\text{init}}$	α_ε (cm/kV)	$\alpha_\varepsilon/\varepsilon_{\text{init}}$ (10^{-3} cm/kV)	Mean (10^{-3} cm/kV)	Std. dev. (10^{-3} cm/kV)
PZT 20/80	161.3 ± 0.1	0.78 ± 0.01	4.8 ± 0.1	-0.66 ± 0.03	1.73
PZT 45/55 [27]	428.0 ± 0.2	6.79 ± 0.05	15.9 ± 0.1	1.84 ± 0.07	5.06
PZT 52/48	793.7 ± 0.8	2.81 ± 0.14	3.5 ± 0.2	-1.56 ± 0.02	1.46

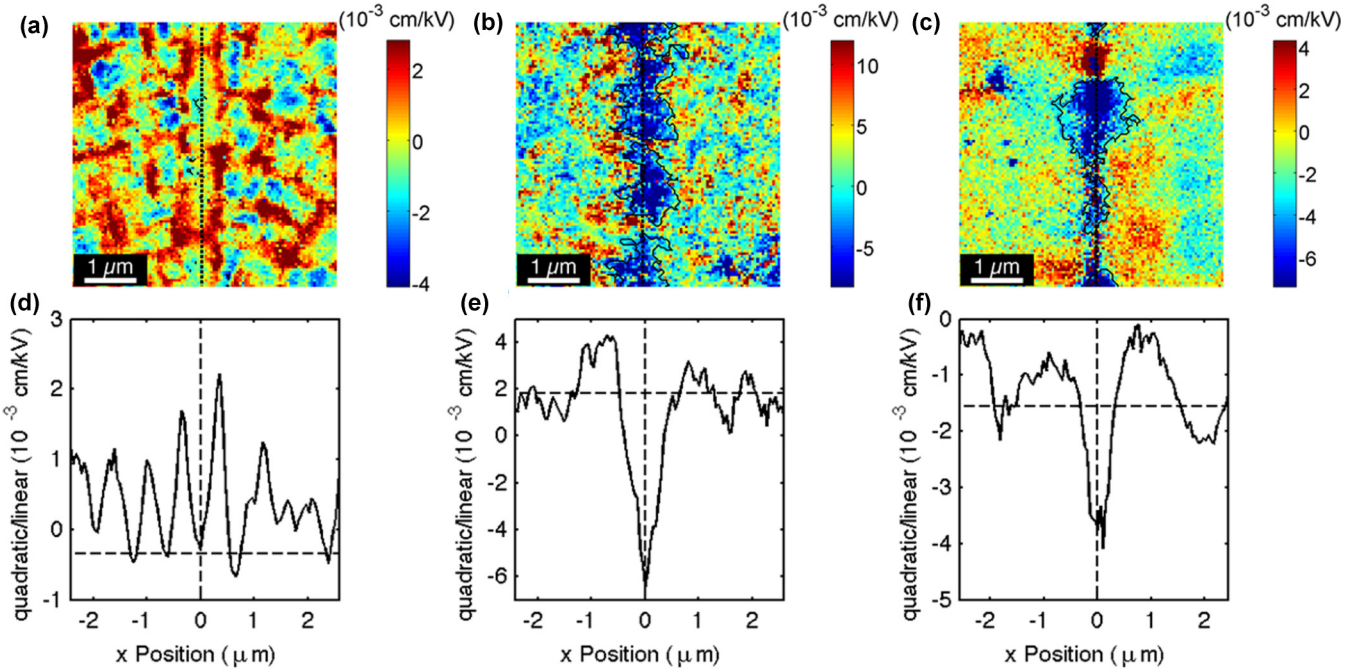

FIG. 1. (Color online) Nonlinear response (quadratic divided by linear response) maps measured across the 24° grain boundary for (a) PZT 20/80, (b) PZT 45/55, and (c) PZT 52/48. Dotted lines denote the location of the grain boundary and solid lines border the regions of low response across the boundary. Plots (d–f) show the nonlinear response quadratic and linear for maps averaged across y positions where (d) corresponds to map (a), (e) corresponds to map (b), and (f) corresponds to map (c). The vertical line denotes the grain boundary and the horizontal line is the off-boundary average nonlinear response. (b,d) from [27].

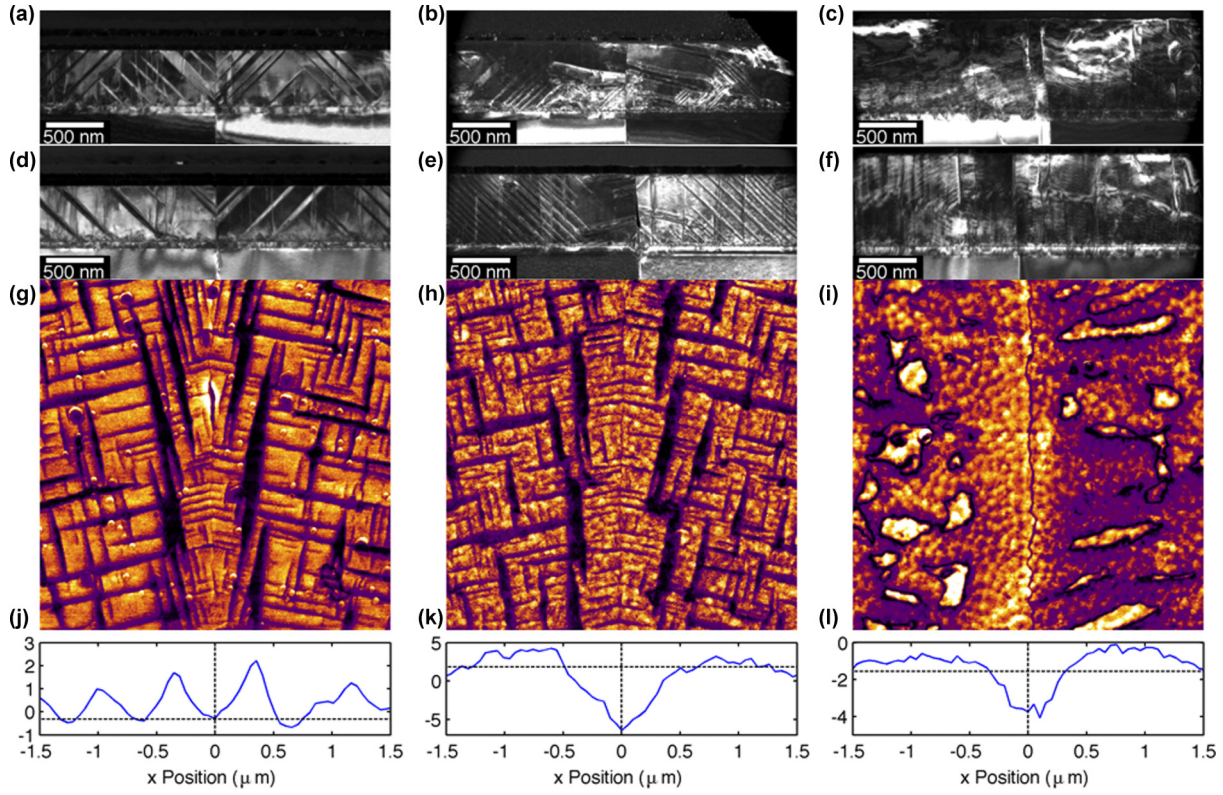

FIG. 2. (Color online) Bright-field cross-section TEM (a–c) unpoled and (d–f) poled PZT, (g–i) vertical PFM amplitude showing out-of-plane (bright) vs in-plane (dark) domains, and (j–l) mean nonlinear response in 10^{-3} cm/kV. Figures (a,d,g,j) PZT 20/80, (b,e,h,k) PZT 45/55, and (c,f,i,l) PZT 52/48. All figures have the same lateral scale with a total width of 3 μm. The 24° grain boundary is located at $x = 0$.

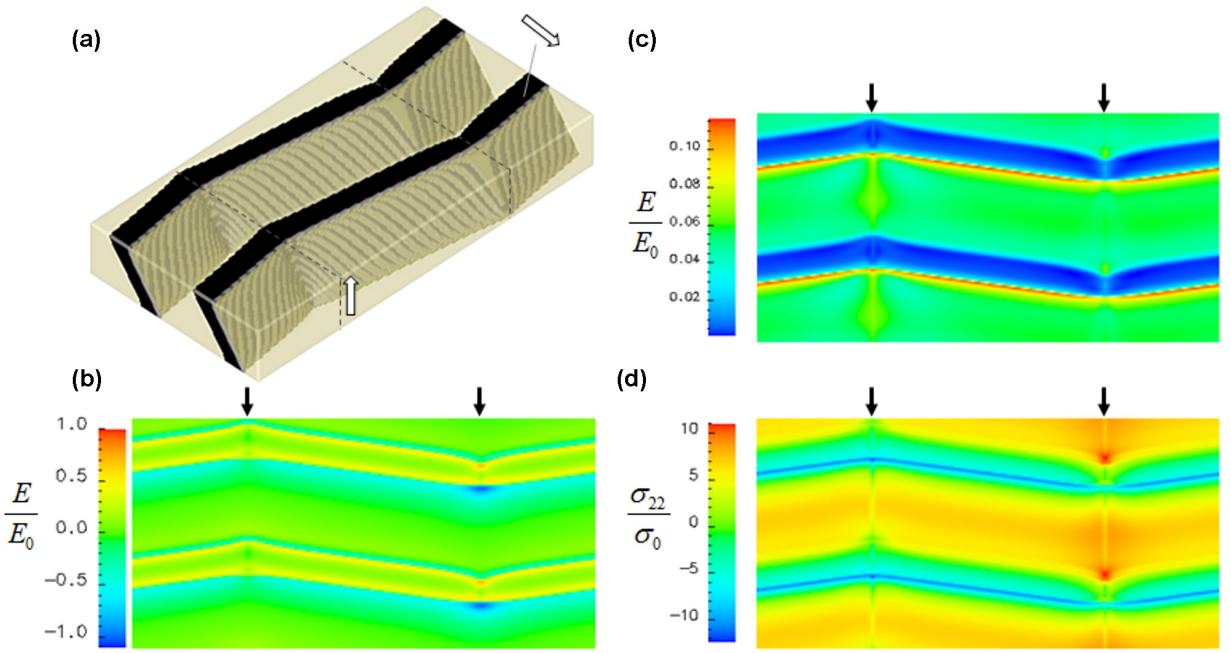

FIG. 3. (Color online) (a) Phase field simulation of stable domain configuration for the a/c domain structure. (b) Electric energy at the top surface of the film structure. (c) Elastic energy at the top surface of the film structure. (d) In-plane σ_{22} stress around the grain boundaries. $\sigma_0 = 93.1$ MPa. The grain boundaries are marked by (a) dashed lines and (c,d) black arrows.

top and bottom surfaces of the film. This produced a wider domain near one boundary, but a narrower domain at the other grain boundary. A minimum in the local electric energy was associated with both boundaries where the domains met across the grain boundary. The reduction in the electric energy is particularly strong at the grain boundary where the domains form a domain wall with a slight tail-to-tail arrangement. Both boundaries, however, are associated with moderate increases in the local elastic energy and stresses within the a domains, as can be seen in Figs. 3(b) and 3(c). Increases in the elastic stresses and energy are larger for the tail-to-tail domain arrangement, indicating that the head-to-head arrangement, associated with an increased domain thickness, is more stable [Figs. 3(c) and 3(d)].

Analysis of the poled domain structure in Fig. 2(d), for which the polarization directions are known, shows b domains increasing in thickness near the grain boundary by ∼10 nm for the head-to-head configuration in PZT 20/80. This agrees with the phase field analysis of head-to-head a-domains increasing in width near the grain boundary. Combined with the decreased energy calculated for the a/c domain configuration by the phase field method, the broadening of the head-to-head domain configuration seen in the microstructure indicates this is more stable than either the tail-to-tail configuration or pure c domain across the boundary.

A similar model consisting of the b/c domain structure observed in PZT 20/80 thin films was considered (Fig. 4). Charged domain interfaces at the grain boundary were assumed in this model to be completely compensated by free charges by ignoring the contribution from the electrical energy to the free energy of the system. A b/c domain structure was seeded, so as to minimize elastic energy and produce a coherent interface. However, after evolution, the phase field model did not reproduce a stable b/c configuration at the grain boundary. Rather, the b/c domain structures observed in TEM [Figs. 2(a)] rapidly transformed to a single c domain adjacent to the grain boundary due to compressive σ_{11} stress and elastic energy concentration at the grain boundary. The lack of stabilization of the domain structures at the grain boundary despite the apparent elastic matching and implicit removal of bound charge in the model indicates an additional stabilization mechanism for this domain structure in the 20/80 PZT film specimen. This suggests that the observed b/c

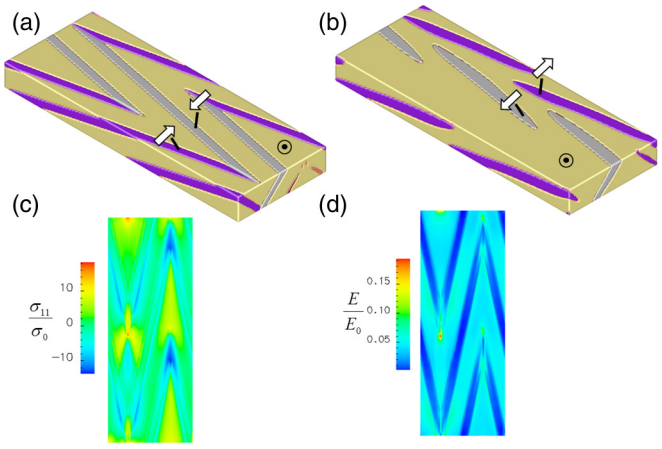

FIG. 4. (Color online) (a) Domain structure of film with head-to-head and tail-to-tail b/c domain structure after 100 time steps. (b) b/c domain structure after partial relaxation (14 000 time steps) showing b domains retreating from the grain boundaries to produce a uniform c domain around the grain boundaries. (c) In-plane σ_{11} stress around the domains. $\sigma_0 = 93.1$ MPa. (d) Elastic energy at top surface of thin film showing elevated elastic energy within the b domain around the grain boundaries.

domain structure is likely stabilized by charged, segregated impurities at the grain boundary or grain boundary dislocations required for mechanical matching across the interface. As shown in Fig. 4, any additional stabilization mechanism in the thin film likely occurs near the sharp intersection of the *b* domains across the boundary and correspond with the local stress concentrations. Dislocations [40,41] have frequently been observed at domain walls in previous high-resolution studies of ferroelectric domain walls and grain boundaries. Additionally, solute segregation at grain boundaries may create negative immobile charges that favor head-to-head domain arrangements. Such defects, if present, will likely pin the domain walls through strong attractive elastic and electrostatic interactions to reduce their overall mobility. Pinning associated with either elastic or electrostatic defects at the grain boundary could reduce the piezoelectric response near the grain boundary as observed in this work.

IV. DISCUSSION

It is clear from Fig. 1 that for the rhombohedral PZT 52/48, the 24° tilt grain boundary influences the mobility of domain walls over a much shorter spatial scale than is the case for the analogous grain boundary in PZT 45/55. Given the significant differences in domain wall density (see Fig. 2), the difference in the width of influence for the grain boundary is attributed to improved strain relaxation for the rhombohedral sample, based on the fine domain structure observed by TEM.

For the tetragonal films, while PZT 45/55 exhibits a well-defined minimum in the nonlinearity at the grain boundary, an alternating nonlinear response was observed for PZT 20/80. These differences are attributed to the disparate poled domain structures. For PZT 20/80, ferroelastic strain matching at the grain boundary permits registry of domain walls between *b* and *c* domains [see Figs. 2(a) and 2(d)] as described previously [27]. From Fig. 5(b), to maintain a head-to-tail domain configuration within each grain there must be a polarization discontinuity at the grain boundary for either the *b* or *c* domains. The PFM lateral phase measurements collected on a virgin region in Fig. 5(c) show a polarization discontinuity in the in-plane polarization at the grain boundary, indicating that the *b* domains at the grain boundary have nearly antiparallel polarizations.

Figure 2(d) shows *b* domains from one side of the boundary bordered either by *b* or *c* domains on the other side, depending on location. A similar observation can be made for *a* domains at the grain boundary in Fig. 2(e). The case where *b* domains border *b* domains at the grain boundary minimizes the local strain energy. However, charge accumulation is required to compensate the primarily head-to-head domain configuration for *b* domains. The intersection of *b* and *c* domains at the grain boundary minimizes charge accumulation, but results in uncompensated local strain.

Note that *b* domains are preferred at the grain boundary for the PZT 20/80 case [Figs. 2(a) and 2(d)], while *a* domains are preferred for the PZT 45/55 case [Figs. 2(b) and 2(e)]. It is anticipated that the formation of the ferroelastic domain structures near the grain boundary is driven by strain accommodation for both the PZT 45/55 and the PZT 20/80 systems. For PZT 20/80, the energy required to form charged defects is lower than for Zr-rich samples due to the decreased band gap [42], leading to the formation of *b* domains to compensate the presence of local charge. Conversely, the larger band gap for PZT 45/55 makes it more difficult to compensate highly charged domain walls, with the result that *a* domains will be preferred over *b* domains at the grain boundary. Evidence of charge carriers in PZT 20/80 is provided by high field hysteresis measurements showing an increased loss compared to PZT 45/55. The influence of electric field on domain structure was previously determined to decay within 100 nm of a charged grain boundary [43], indicating that any charge accumulation at the grain boundary is quickly compensated by the local domain structure.

Comparison between the domain structures of PZT 20/80 before and after poling in Figs. 2(a) and 2(d) indicates that a decreased concentration of *b* domains is present within 500 nm of the grain boundary after poling. To better understand the poling process, consider a *b* domain near the grain boundary on poling. Due to the elastic constraints imposed by the substrate, the *b* domain is unable to completely switch to *c* domain. However, by moving the domain to intersect the grain boundary, the total volume of *c* oriented polarization will increase by decreasing the *b* domain concentration *adjacent* to

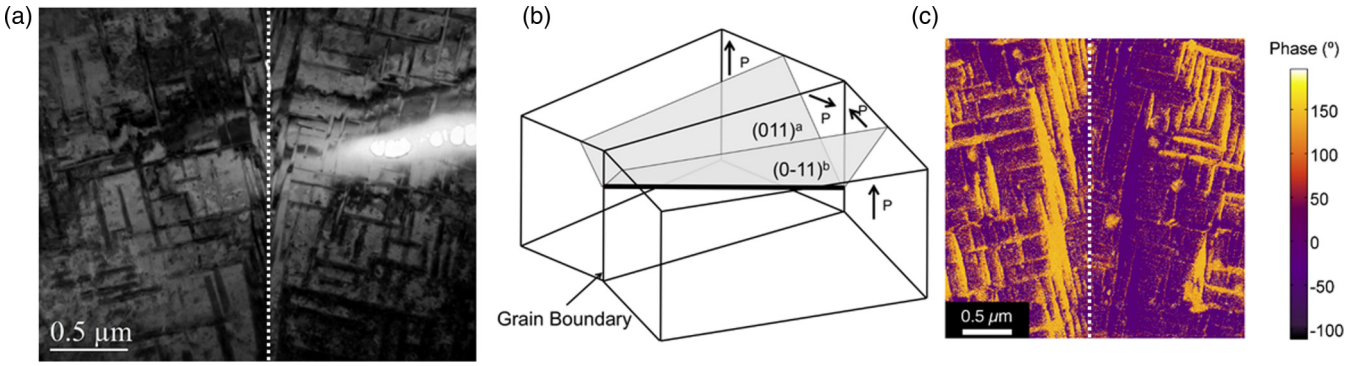

FIG. 5. (Color online) (a) Plan-view TEM of PZT 20/80 unpoled region showing similar domain structure to vertical PFM in Fig. 2(g). (b) Schematic of domain wall strain matching at the grain boundary showing how (011) type 90° domain walls from each grain intersect to minimize strain at the grain boundary with head-to-head polarization. (c) Lateral PFM of PZT 20/80 showing in-plane polarization reversal at the grain boundary. (a,c) The vertical dashed lines denote the grain boundary.

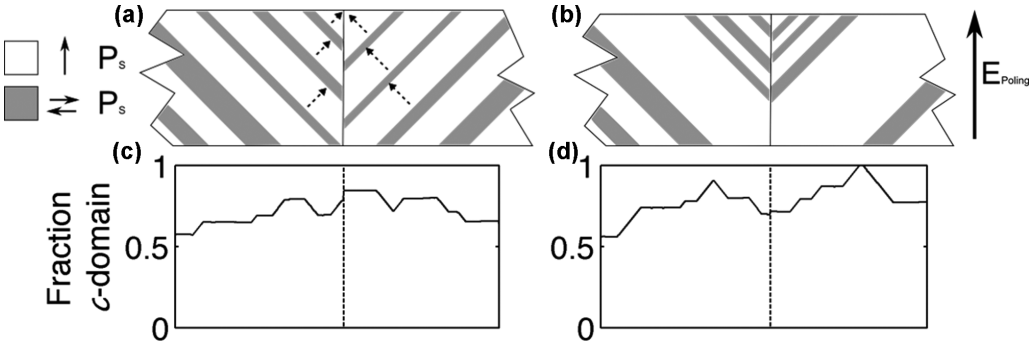

FIG. 6. Schematic of how the *c*-domain volume near the grain boundary increases when poled with an electric field in the *c* direction. (a) The unpoled domain structure with dotted arrows showing the direction of domain movement on (b) poling. Shaded regions indicate *b* domains while white regions indicate *c* domains. (c,d) *c*-domain fraction with distance from the grain boundary (c) before and (d) after poling.

the grain boundary, as shown in Fig. 2(d). In some regions, the *b* domains may be completely removed. A schematic illustrating this is shown in Fig. 6. In contrast, *a* domains move nearly parallel to the grain boundary, such that only modest volume can be converted to *c* orientation in the same manner.

Further insight into the poling behaviors of the two domain structures can be gained by consideration of the relative domain stabilities from the phase field simulations. Phase field modeling indicates that the ferroelastic domain structure at the grain boundary in the PZT 20/80 sample is not intrinsically stable, but is rather stabilized by defects in the system. The permanent reduction in the concentration of ferroelastic *b* domains observed in PZT 20/80 upon poling indicates the system energy can be reduced despite the role they play in elastic strain compensation. The applied electric field must therefore be large enough to dissociate the domain walls from local pinning centers at the grain boundaries. The original grain boundary arrangement does not return when the poling field is removed since, as indicated in the phase field simulation, increases in the *b*-domain fraction at the grain boundary raises the total system energy.

In contrast, ferroelastic *a* domains at the grain boundary in PZT 45/55 are particularly stable in the phase field simulation and reduce the overall system energy. Broadening of *a* domains at the boundary indicate their presence is particularly stable. When the structure is poled, the low-energy domain structure and stable ferroelastic interfaces must be removed in addition to displacing domain walls from their local pinning centers. As a result, the PZT 45/55 structure is expected to be more difficult to pole than the PZT 20/80 structure as based on the free energy and structure calculations in the phase field model and agreeing with the experimentally determined poling field.

No global minimum in the nonlinear response is observed at the grain boundary for PZT 20/80. Rather, a striped pattern in the nonlinear response is evident; the striping is not observed far from the grain boundary (Fig. 7), although clustering of high- and low-response regions is evident. It is likely that the striped nonlinear response is due to changes in the domain structure associated with accommodation of the strain and electric fields at the grain boundary. Although the domain structure is unknown for the region in which the nonlinear response was collected, comparison can be made between the *average* nonlinear response and *average* domain structure at specific distances from the grain boundary.

For PZT 20/80, a maximum in nonlinear response occurs in Fig. 2(j) at ∼360 nm to either side of the grain boundary, similar to that observed for PZT 45/55 [27]. The domain structure for the poled region in Fig. 2(d) shows that the maximum in nonlinear response corresponds to the edge of a region primarily consisting of *c* polarization, where *a* and *b* domains intersect the substrate. One possibility is that the maximum in nonlinear response results because the 90° domain walls can move irreversibly into the *c*-polarized region due to reduced interaction with other 90° domain walls and to reduce the elastic strain present in the pure *c*-domain region of the thin film. Contributions from 180° domain wall motion, if present within the large *c*-polarized region,

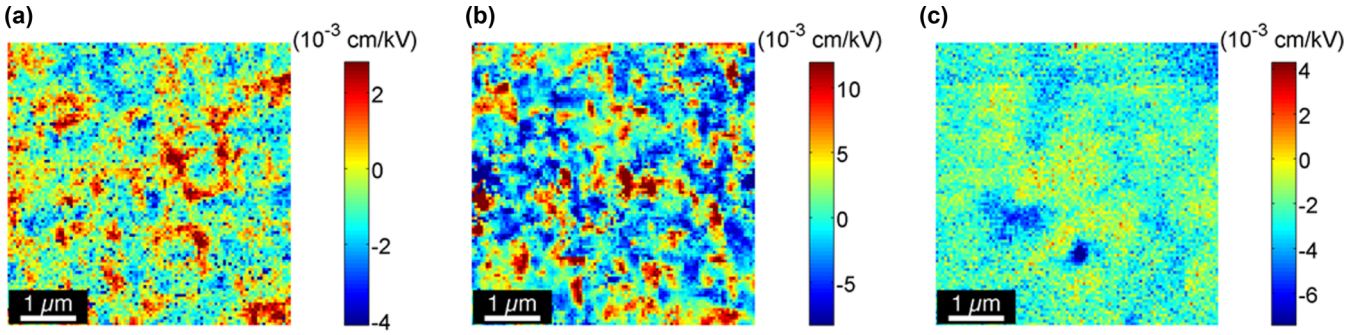

FIG. 7. (Color online) Nonlinear response (quadratic divided by linear response) maps measured far from the grain boundary for various compositions (a) PZT 20/80, (b) PZT 45/55, and (c) PZT 52/48.

may further increase the nonlinear response as described elsewhere [44,45]. Furthermore, a minimum occurs in the nonlinear response in Fig. 2(j) at ∼650 nm to either side of the grain boundary. At this distance, Fig. 2(d) shows an increased volume fraction of in-plane polarization relative to regions closer to the grain boundary. A decreased nonlinear response when a larger number of 90° domain walls are present suggests 90° domain wall–domain wall pinning.

A similar maximum is observed near the grain boundary for PZT 52/48 in Fig. 2(l). No variation in domain structure or configuration can be identified in Fig. 2(f) due to the small domain size. However, the maximum in nonlinear response corresponds to the introduction of 180° domain walls in Fig. 2(i). Although the PFM data were collected on an unpoled region, it is anticipated that some variation in the average domain structure through the thickness of the film is still present at this position after poling.

V. CONCLUSIONS

A 24° tilt grain boundary was found to have maximum influence on pinning domain wall movement for {001} oriented epitaxial PZT 45/55, followed by PZT 52/48 and PZT 20/80. The reduced influence of the grain boundary on pinning for PZT 52/48 was attributed to the higher domain wall density accommodating the local strain and electric fields. The effect of the grain boundary on domain wall motion for PZT 20/80 was more complex, with alternating low and high nonlinear response as a function of distance from the grain boundary associated with the local domain structure.

Domain wall pinning was attributed to the local elastic and electric fields at the grain boundary, as shown in the phase field model, and the local domain structure, observed by TEM and PFM. There is a strong indication that domain wall–domain wall pinning plays an important role in the evolution of global properties in ferroelectric materials. Such a combination of characterization techniques can be used to study other pinning sources, such as defect dipoles and isolated dislocations.

This work provides insight for the development of macroscopic properties from the nanoscale properties in multiple material systems, including ferromagnets and ferroelastics. The results displayed here can be used as a starting point to model the behavior of domain wall interactions and the evolution of functional properties in polycrystalline materials.

ACKNOWLEDGMENTS

Support for this work was provided in part by the National Science Foundation Grant No. DMR-1005771 (D.M. and S.T.M.). H.R.Z., I.R., and W.M.R. would like to acknowledge funding from the Engineering and Physical Sciences Research Council Grant No. EP/I038934/1. Band excitation piezoresponse force microscopy was conducted at the Center for Nanophase Materials Sciences under user proposal CNMS2011-022, which is sponsored at Oak Ridge National Laboratory by the Scientific User Facilities Division, Office of Basic Energy Sciences, U.S. Department of Energy. The theoretical component of this work at the Pennsylvania State University was supported by the U.S. Department of Energy, Office of Basic Energy Sciences, Division of Materials Sciences and Engineering under Award No. FG02-07ER46417 (J.B. and L.Q.C.). Calculations at the Pennsylvania State University were performed on the Cyberstar Linux Cluster funded by the National Science Foundation through Grant No. OCI-0821527.

APPENDIX A: RAYLEIGH ANALYSIS

The Rayleigh law describes the change in dielectric and piezoelectric response with increasing subcoercive ac electric field:

$$\varepsilon_r = \varepsilon_{\text{init}} + \alpha_\varepsilon E_0, \tag{A1}$$

$$d_{33} = d_{33,\text{init}} + \alpha_d E_0. \tag{A2}$$

For Eqs. (A1) and (A2), ε_r and d_{33} are the relative permittivity and piezoelectric constant, $\varepsilon_{\text{init}}$ and $d_{33,\text{init}}$ are the reversible components of the permittivity and piezoelectric response, relating to the intrinsic contribution and reversible movement of domain walls, α_ε and α_d are the irreversible components relating to irreversible movement of domain walls across pinning sites, and E_0 is the magnitude of the ac electric field. The Rayleigh law holds as long as the response is dominated by movement of existing domain walls in a Gaussian distribution of restoring forces, and not by nucleation and growth of new domains. For many ferroelectric materials, the Rayleigh law is applicable up to one third to one half of the coercive field [46].

APPENDIX B: METHODS FOR ANALYZING CLUSTERS OF NONLINEAR RESPONSE

Clusters of high and low nonlinear response were observed, as has been reported previously [47], where the clustered regions were defined as being above or below the mean nonlinear response $\pm\frac{1}{2}$ standard deviation measured far from the grain boundary. Most low-response pixels were observed at the grain boundary. Three methods were used to determine the width of influence for a grain boundary on the nonlinear response of a PZT thin film. The reported widths of influence and confidence intervals reflect all analysis methods. Values for all three methods are reported for PZT 45/55 and PZT 52/48 in Table III. A description of each method follows.

Method 1: The mean and standard deviations in the nonlinear response for each sample were determined from maps collected far (∼5 mm) from the grain boundary. Low-response pixels were considered to be statistically significant if the value was more than half a standard deviation below the mean nonlinear response. Clusters were counted if they contained at least four contiguous pixels. The total area enclosed in low-response regions crossing the grain boundary was then

TABLE III. Width of influence of grain boundary in μm as determined by 3 different methods.

Composition	Method 1	Method 2	Method 3
PZT 45/55	0.722 ± 0.056	0.870 ± 0.044	0.837 ± 0.041
PZT 52/48	0.429 ± 0.088	0.421 ± 0.056	0.476 ± 0.016

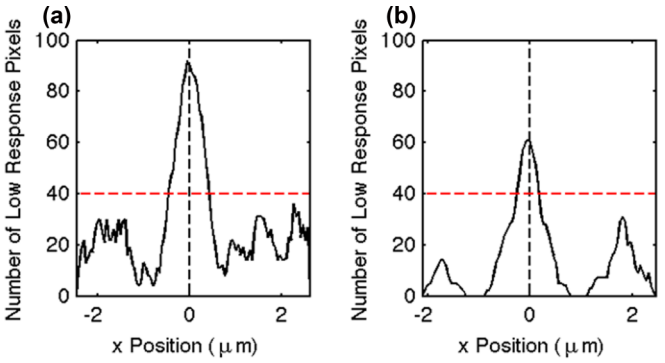

FIG. 8. (Color online) Number of low-response pixels varying with distance from the grain boundary for (a) PZT 45/55 and (b) PZT 52/48. The red horizontal line marks the cutoff determined by 40 low-response pixels out of 100 total pixels, while the black vertical line denotes the grain boundary.

divided by the total length of the grain boundary measured (5 μm) in order to determine an average width of influence. The error bars were determined as the 95% confidence in the width of low response at each row. This method does not take into consideration the spatial distribution of low-response regions, which Method 2 considers, yet it better reflects the averaged *low* response.

Method 2: Using all low-response clusters on the map of the grain boundary as determined in Method 1, the number of low-response pixels observed with distance from the grain boundary was represented in a histogram (see Fig. 8). If a random distribution of the nonlinear response were observed with no clustering, approximately 30% of the pixels at each distance from the grain boundary should be low response. Due to clustering in the response, the cutoff value was set to 40% of the pixels observed at each distance from the grain boundary being low response. The error bars were determined as ±5% in the ratio of low-response pixels. This method does not account for high-response regions at the grain boundary, which Method 3 considers, yet it better reflects the spatial distribution of *low*-response regions compared to Methods 1 and 2.

Method 3: The average of the nonlinear response parallel to the grain boundary shows a minimum at the grain boundary. A cutoff value of 25% of the standard deviation below the mean nonlinear response was used to determine the width of influence, as shown in Fig. 9. Error bars were determined as ±5% in the average nonlinear response. This method considers the contribution of high-response regions at and near the grain boundary, which Methods 1 and 2 do not consider. This method provides a better understanding of how the nonlinear response changes with distance from the grain boundary but is inferior at analyzing how low nonlinear response clusters at the grain boundary.

APPENDIX C: PHASE FIELD MODEL

Phase field modeling was used to simulate the equilibrium domain structure around the grain boundaries to gain additional insight into local electric and stress fields caused by domain interactions across the grain boundary. This approach numerically minimizes the total free energy, F, of the thin film with respect to the distribution of the polarization, P_i, by iteratively solving the time-dependent Ginzburg-Landau equation [13,34,35],

$$\frac{\partial P_i}{\partial t} = -L\frac{\delta F}{\delta P_i} \tag{C1}$$

as discussed in previous publications [36] to evolve the polarization distribution to a local minimum in the free energy from a specified initial condition. The free energy in this model contained contributions from the bulk free energy of the crystal, the electrostatic free energy of electric dipole interactions, the mechanical free energy of internal stress fields, and the gradient free energy around changes in the polarization in the PZT thin film. Altogether, the free energy of the thin film was expressed as [34]

$$F(P_i, E_i, \varepsilon_{ij}) = \iiint_V (f_{\text{bulk}} + f_{\text{electric}} + f_{\text{mechanical}} + f_{\text{gradient}})dV. \tag{C2}$$

In this model, effects due to surface and interface energies were neglected for simplicity. The bulk free energy of PZT in the tetragonal polarization state was modeled using the sixth-order Landau polynomial,

$$f_{\text{bulk}} = \frac{\alpha_i(T)}{2}P_i^2 + \frac{\beta_{ij}}{4}P_i^2P_j^2 + \frac{\gamma_{ijk}}{6}P_i^2P_j^2P_k^2, \tag{C3}$$

with coefficients α_i, β_{ij}, and γ_{ijk}, measured by Haun *et al.* [48] for the free energy functional at room temperature. In Eq. (C3) the leading coefficient, α_i, is a function of temperature to reproduce the paraelectric to tetragonal ferroelectric transition in PZT.

Electrical interactions between electric charges in the film were modeled with the equation [37]

$$f_{\text{electric}} = -E_iP_i - \tfrac{1}{2}\kappa_{ij}E_iE_j, \tag{C4}$$

where κ_{ij} is the background dielectric constant of the thin film independent of the polarization state [49] and E_i are the components of the electric field. Electric fields were

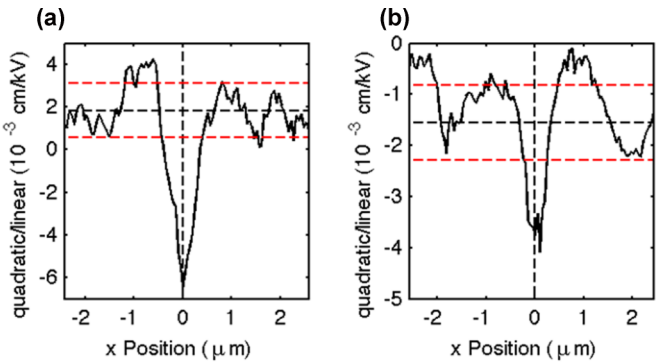

FIG. 9. (Color online) Nonlinear response averaged parallel to the grain boundary for (a) PZT 45/55 and (b) PZT 52/48. The black vertical line denotes the location of the grain boundary, while the black horizontal line shows the mean nonlinear response and the red horizontal lines indicate ±25% of the standard deviation.

determined by solving the Poisson equation,

$$\frac{\partial}{\partial x_i}\left(\kappa_{ij}\frac{\partial \varphi}{\partial x_j}\right) = \rho_f - \frac{\partial P_i}{\partial x_i}, \tag{C5}$$

for the electric potential distribution, φ, at each iteration of the time-dependent Ginzburg-Landau equation solution. In Eq. (C5) the first term on the right-hand side of the equation, ρ_f, is the charge due to the carrier concentration and the second term is the bound charge due to changes in the polarization distribution. Electrical behavior in the thin film was determined by the conditions used to solve Eq. (C5). For PZT 45/55, the band gap is large, and thus the concentration of charge carriers was assumed to be negligible. In this case, all of the system charge was the result of the bound charge. In contrast, for the narrower band gap PZT 20/80 a higher concentration of carrier charges was assumed to exactly cancel the bound charge, which removed charge dipoles and electric fields from the thin film. While the PZT 20/80 system likely supports some uncompensated bound charges even at the grain boundary, this assumption was based on the observation of head-to-head domain configurations at the grain boundary. It was anticipated that a high concentration of bound charge would be required to stabilize such a structure.

Mechanical interactions due to the spontaneous deformation of the ferroelectric crystals below the transition temperature were modeled as [35,50]

$$f_{\text{mechanical}} = \tfrac{1}{2}\sigma_{ij}\left(\varepsilon_{ij} - \varepsilon^0_{ij}\right), \tag{C6}$$

where σ_{ij} and ε_{ij} are the mechanical stress and strain in the system, respectively, and ε^0_{ij} is the stress-free strain associated with spontaneous strain of the crystal [51]. Stress in the system was found by solving the mechanical equilibrium equation,

$$\frac{\partial \sigma_{ij}}{\partial x_j} = 0, \tag{C7}$$

where the stress is related to the strain through $\sigma_{ij} = C_{ijkl}(\varepsilon_{kl} - \varepsilon^0_{kl})$. Elastic constants measured by Haun *et al.* for tetragonal PZT were used in the simulation. Like the electrostatic problem, the mechanical state of the system was determined from the boundary conditions of Eq. (C7). In order to model the thin film system, the out-of-plane components of the stress were assumed to be zero at the top surface of the thin film. At the bottom of the epitaxial thin film, however, the substrate constrains the film so that the surface is not traction free. Rather, the substrate relaxes for a small distance into the substrate before the displacement of the substrate is zero. As a result, the mechanical displacement at the bottom of the simulation volume was assumed to be zero [35]. Some nonpolarizable layers of substrate were included between the bottom of the simulation volume and the bottom of the thin film. For simplicity, the substrate and thin film were assumed to have identical elastic constants.

Finally, the gradient energy was included to incorporate the domain wall energy in the system with the equation

$$f_{\text{gradient}} = \frac{1}{2}G_{ijkl}\frac{\partial P_i}{\partial x_j}\frac{\partial P_k}{\partial x_l}, \tag{C8}$$

where G_{ijkl} is the gradient energy tensor. For the sake of simplicity, the domain wall energy was assumed to be isotropic, reducing the expression for the gradient energy to [35]

$$f_{\text{gradient}} = \frac{1}{2}G_{1111}\sum_{i=1}^{3}\sum_{j=1}^{3}\left(\frac{\partial P_i}{\partial x_j}\right)^2. \tag{C9}$$

The gradient energy coefficient used was assumed to have a value of $4.1 \times 10^{-11}\ \text{C}^{-2}\ \text{m}^4\ \text{N}$. This choice has been shown to lead to a 90° domain wall width of 1–2 nm, in reasonable agreement with experimental observations [18,41].

The bicrystal was modeled by assuming the constants used to find the bulk energy [Eq. (C3)] and the elastic constants rotated across the grain boundary. The rotation of the constants was assumed to be linear across the grain boundary. The rotation at the grain boundary was set to occur over a grain boundary width of 2 nm. This approach, however, does not account for possible other changes in the properties of the system at the boundary. It was determined that the approximation used was sufficient since many of the resulting models were consistent with the experimental observations.

While phase field models have been shown to accurately reproduce both equilibrium domain structures [52,53] and dynamic domain responses [17,54] under applied electric and elastic fields, some assumptions made in the model must be fully understood to correctly interpret results. Perhaps most importantly, phase field models assume that the polarization, electric fields, and stresses vary smoothly and continuously across internal interfaces such as domain walls in the thin film [36,38,55]. In order to ensure numerical stability of the calculations, the thickness of the transition regions must be on the same length scale as the grid spacing. As a result, the domain wall widths are often overestimated or only relatively small systems can be simulated. Here, we have decided to use a small system in order to reproduce a physically reasonable domain wall width since one primary goal of the simulation is to understand how the finite domain wall width changes the electrostatic and mechanical fields around the grain boundary to influence the relative stability of the domain structures.

The small system results in strong interactions between the grain boundaries. This is in contrast to the experimental system where the grain boundaries are essentially isolated and individual in-plane domains interact primarily with other domains with in-plane polarization, rather than the next grain boundary, as occurs in the phase field simulations. While this may cause some interactions to be overlooked, the phase field model provides information about the electric fields and stresses around the grain boundary that strongly influence the domain wall mobility and stability.

Further, the phase field model is a continuous model that neglects the variation in the crystal potential due to the lattice in real systems. This effect can make domain walls appear more mobile than is shown to be the case experimentally [56]. No changes should occur with the stability of the domains, however, so that this effect only eliminates metastable domain states more quickly than experimental systems. Since the simulations were performed to understand the stable domain configurations, the additional mobility of the domain walls due to the continuous nature of the model is not a significant limitation.

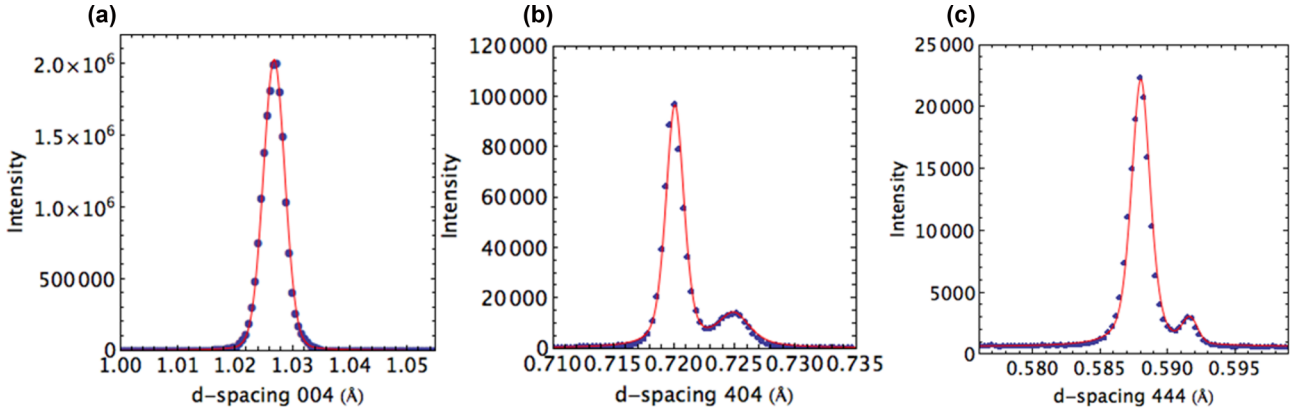

FIG. 10. (Color online) Rod scans on the (a) 004, (b) 404, and (c) 444 peaks of PZT 52/48.

APPENDIX D: PHASE OF PZT 52/48

Synchrotron x-ray diffraction was conducted to determine the phase of the PZT 52/48 films. Measurements were collected on 004, 404, and 444 peaks and are shown in Fig. 10. Splitting was observed in the 444 and 404 peaks, with no splitting observed in 004. This corresponds to a rhombohedral structure [57].

[1] G. Arlt, Ferroelectrics **91**, 3 (1989).
[2] W. Cao and C. A. Randall, J. Phys. Chem. Solids **57**, 1499 (1996).
[3] J. F. Scott, J. Phys. Condens. Matter **26**, 212202 (2014).
[4] N. Setter, D. Damjanovic, L. Eng, G. Fox, S. Gevorgian, S.-K. Hong, A. I. Kingon, H. Kohlstedt, N. Y. Park, G. B. Stephenson, I. Stolichnov, A. K. Tagantsev, D. V. Taylor, T. Yamada, and S. K. Streiffer, J. Appl. Phys. **100**, 051606 (2006).
[5] G. Arlt, D. F. Hennings, and G. de With, J. Appl. Phys. **58**, 1619 (1985).
[6] M. Demartin and D. Damjanovic, Appl. Phys. Lett. **68**, 3046 (1996).
[7] C. A. Randall, N. Kim, J.-P. Kucera, W. Cao, and T. R. Shrout, J. Am. Ceram. Soc. **81**, 677 (1998).
[8] D. Damjanovic and M. Demartin, J. Phys.: Condens. Matter **9**, 4943 (1997).
[9] D. A. Hall, A. Steuwer, B. Cherdhirunkorn, T. Mori, and P. J. Withers, J. Appl. Phys. **96**, 4245 (2004).
[10] J. F. Ihlefeld, A. M. Vodnick, S. P. Baker, W. J. Borland, and J.-P. Maria, J. Appl. Phys. **103**, 074112 (2008).
[11] F. Griggio and S. Trolier-McKinstry, J. Appl. Phys. **107**, 024105 (2010).
[12] S. Choudhury, Y. Li, C. Krill III, and L.-Q. Chen, Acta Mater. **53**, 5313 (2005).
[13] S. Choudhury, Y. L. Li, C. Krill III, and L.-Q. Chen, Acta Mater. **55**, 1415 (2007).
[14] W. Zhang and K. Bhattacharya, Acta Mater. **53**, 199 (2005).
[15] R. E. García, B. D. Huey, and J. E. Blendell, J. Appl. Phys. **100**, 064105 (2006).
[16] P. Marton, T. Shimada, T. Kitamura, and C. Elsässer, Phys. Rev. B **83**, 064110 (2011).
[17] P. Gao, J. Britson, J. R. Jokisaari, C. T. Nelson, S.-H. Baek, Y. Wang, C.-B. Eom, L.-Q. Chen, and X. Pan, Nat. Commun. **4**, 2791 (2013).
[18] B. Meyer and D. Vanderbilt, Phys. Rev. B **65**, 104111 (2002).
[19] T. Tybell, P. Paruch, T. Giamarchi, and J.-M. Triscone, Phys. Rev. Lett. **89**, 097601 (2002).
[20] P. Paruch, T. Giamarchi, T. Tybell, and J.-M. Triscone, J. Appl. Phys. **100**, 051608 (2006).
[21] P. Paruch, A. B. Kolton, X. Hong, C. H. Ahn, and T. Giamarchi, Phys. Rev. B **85**, 214115 (2012).
[22] B. D. Huey, R. Nath, S. Lee, and N. A. Polomoff, J. Am. Ceram. Soc. **95**, 1147 (2012).
[23] Y. Kim, Y. Cho, S. Hong, S. Bühlmann, H. Park, D.-K. Min, S.-H. Kim, and K. No, Appl. Phys. Lett. **89**, 172909 (2006).
[24] B. J. Rodriguez, Y. H. Chu, R. Ramesh, and S. V. Kalinin, Appl. Phys. Lett. **93**, 142901 (2008).
[25] H. Chang, S. V. Kalinin, S. Yang, P. Yu, S. Bhattacharya, P. P. Wu, N. Balke, S. Jesse, L. Q. Chen, R. Ramesh, S. J. Pennycook, and A. Y. Borisevich, J. Appl. Phys. **110**, 052014 (2011).
[26] Y. Ivry, D. Chu, J. F. Scott, and C. Durkan, Adv. Funct. Mater. **21**, 1827 (2011).
[27] D. M. Marincel, H. Zhang, A. Kumar, S. Jesse, S. V Kalinin, W. M. Rainforth, I. M. Reaney, C. A. Randall, and S. Trolier-McKinstry, Adv. Funct. Mater. **24**, 1409 (2014).
[28] A. Pramanick, J. E. Daniels, and J. L. Jones, J. Am. Ceram. Soc. **92**, 2300 (2009).
[29] A. Pramanick, D. Damjanovic, J. C. Nino, and J. L. Jones, J. Am. Ceram. Soc. **92**, 2291 (2009).
[30] F. Griggio, S. Jesse, W. Qu, A. Kumar, O. Ovchinnikov, D. S. Tinberg, S. V Kalinin, and S. Trolier-McKinstry, J. Appl. Phys. **110**, 044109 (2011).
[31] D. Damjanovic, J. Am. Ceram. Soc. **88**, 2663 (2005).
[32] B. Jaffe, W. R. Cook, and H. Jaffe, *Piezoelectric Ceramics* (Academic Press, New York, 1971).
[33] D. Damjanovic and M. Demartin, J. Phys. D: Appl. Phys. **29**, 2057 (1996).
[34] L. Q. Chen, J. Am. Ceram. Soc. **91**, 1835 (2008).

[35] Y. L. Li, S. Y. Hu, Z. K. Liu, and L. Q. Chen, Acta Mater. **50**, 395 (2002).
[36] L. Q. Chen and J. Shen, Comput. Phys. Commun. **108**, 147 (1998).
[37] Y. L. Li, S. Y. Hu, Z. K. Liu, and L. Q. Chen, Appl. Phys. Lett. **81**, 427 (2002).
[38] P. Yu, S. Y. Hu, L. Q. Chen, and Q. Du, J. Comput. Phys. **208**, 34 (2005).
[39] G. A. Rossetti and A. G. Khachaturyan, Appl. Phys. Lett. **91**, 072909 (2007).
[40] D. Su, Q. Meng, C. A. F. Vaz, M.-G. Han, Y. Segal, F. J. Walker, M. Sawicki, C. Broadbridge, and C. H. Ahn, Appl. Phys. Lett. **99**, 102902 (2011).
[41] M.-W. Chu, I. Szafraniak, D. Hesse, M. Alexe, and U. Gösele, Phys. Rev. B **72**, 174112 (2005).
[42] C. H. Peng, J.-F. Chang, and S. B. Desu, Mater. Res. Soc. Symp. Proc. **243**, 21 (1992).
[43] W. Heywang, J. Mater. Sci. **6**, 1214 (1971).
[44] S. Trolier-McKinstry, N. Bassiri-Gharb, and D. Damjanovic, Appl. Phys. Lett. **88**, 202901 (2006).
[45] R. K. Vasudevan, M. B. Okatan, I. Rajapaksa, Y. Kim, D. Marincel, S. Trolier-McKinstry, S. Jesse, N. Valanoor, and S. V Kalinin, Sci. Rep. **3**, 2677 (2013).
[46] N. Bassiri-Gharb, I. Fujii, E. Hong, S. Trolier-McKinstry, D. V. Taylor, and D. Damjanovic, J. Electroceram. **19**, 49 (2007).
[47] P. Bintachitt, S. Jesse, D. Damjanovic, Y. Han, I. M. Reaney, S. Trolier-McKinstry, and S. V Kalinin, Proc. Natl. Acad. Sci. USA **107**, 7219 (2010).
[48] M. J. Haun, Z. Q. Zhuang, E. Furman, S. J. Jang, and L. E. Cross, Ferroelectrics **99**, 45 (1989).
[49] A. Tagantsev, Ferroelectrics **69**, 321 (1986).
[50] J. X. Zhang, R. Wu, S. Choudhury, Y. L. Li, S. Y. Hu, and L. Q. Chen, Appl. Phys. Lett. **92**, 122906 (2008).
[51] A. Devonshire, Adv. Phys. **3**, 85 (1954).
[52] N. Balke, B. Winchester, W. Ren, Y. H. Y. Chu, A. N. Morozovska, E. A. Eliseev, M. Huijben, R. K. Vasudevan, P. Maksymovych, J. Britson, S. Jesse, I. Kornev, R. Ramesh, L. Bellaiche, L. Q. Chen, and S. V. Kalinin, Nat. Phys. **8**, 81 (2011).
[53] B. Winchester, P. Wu, and L. Q. Chen, Appl. Phys. Lett. **99**, 052903 (2011).
[54] P. Gao, J. Britson, C. T. Nelson, J. R. Jokisaari, C. Duan, M. Trassin, S.-H. Baek, H. Guo, L. Li, Y. Wang, Y.-H. Chu, A. M. Minor, C.-B. Eom, R. Ramesh, L.-Q. Chen, and X. Pan, Nat. Commun. **5**, 3801 (2014).
[55] H.-L. Hu and L. Q. Chen, J. Am. Ceram. Soc. **81**, 492 (1998).
[56] A. N. Morozovska, E. A. Eliseev, G. S. Svechnikov, and S. V. Kalinin, J. Appl. Phys. **113**, 187203 (2013).
[57] S. Yokoyama, Y. Honda, H. Morioka, S. Okamoto, H. Funakubo, T. Iijima, H. Matsuda, K. Saito, T. Yamamoto, H. Okino, O. Sakata, and S. Kimura, J. Appl. Phys. **98**, 094106 (2005).